Supporting Information:

Rational Design of Organic Diradicals with Robust High-Spin Ground State Based on Antiaromatic Linkers

Raul Santiago, M. Àngels Carvajal, Jordi Poater, Ibério de P. R. Moreira,*

*Stefan T. Bromley, Mercè Deumal, Jordi Ribas-Ariño**

e-mail: raul.sant.1972@gmail.com & j.ribas@ub.edu

S1. Spectral Graph Theory applied to predict trends in ΔE_{ST}

S1.1. General description of the theory

In this section we focus on outlining the Spectral Graph Theory (SGT) methodology employed to pre-screen the frontier Molecular Orbital (MO) topology of the pentalene-like diradicals studied throughout this study. The SGT methodology is tightly bonded to quantum chemistry, specially to Hückel Molecular Orbital (HMO) theory.[1] Thus, we will leverage the interpretability of HMO to demonstrate the potential of SGT in order to extract meaningful insights, assess the MO topology and predict the singlet-triplet gap (ΔE_{ST}) of fully-conjugated (poly-)cyclic hydrocarbons. In HMO, the Hamiltonian of the system, $\widehat{H}$, is expressed in its matrix representation on the basis of p_z^i atomic orbitals (AOs) of the carbon scaffold. Diagonal elements, h_{ii}, are assigned to α, accounting for the energy of the isolated p_z^i AOs. In turn, the off-diagonal elements, h_{ij}, take a value of either β or 0, serving as the resonance integral between adjacent p_z^i and p_z^j AOs or an absence of interaction, respectively. The Hückel MOs can be directly obtained by solving the associated eigenvalue equation, $\widehat{H}C = CE$, where E and C are the matrices representing the MO energies and coefficients, respectively.

The HMO Hamiltonian bears a clear relationship with the adjacency matrix, A, of the graph associated with the carbon scaffold. More precisely, A is identical to $\widehat{H}$ when choosing α = 0 and β = 1. The choice of α leads only to a shift of the sign and value of the MO energies, but β = 1 maintains the same topological atom connectivity and, thus, A yields the exact same MOs than a given $\widehat{H}$ with the same value of β for all the interacting atoms. Following the *Aufbau* and Pauli's exclusion principles, the fully-occupied, partially-occupied, and unoccupied MOs can be straightforwardly obtained from the SGT perspective after diagonalizing the adjacency matrix associated with the carbon atoms of the system.

S1.2. Application of Spectral Graph Theory to Molecular Magnetism

Once the MOs are obtained by SGT, the open-shell character of planar fully-conjugated systems can be assessed upon analyzing the two frontier (potentially) singly-occupied MOs, namely Ψ_a and Ψ_b, and also to their associated energies, E_a and E_b. In non-degenerate cases, $E_a \neq E_b$, the *Aufbau* principle and Pauli's exclusion principle are sufficient to anticipate a closed-shell ground state to a first approximation. However, in the degenerate case, *i.e.* $E_a = E_b$, Hund's rule of maximum multiplicity favors a parallel alignment of the two electrons each in one MO. Despite two frontier MOs can

"accidentally" be degenerate, here we have only focused on the diradicals possessing degenerate orbitals by design. At the HMO/SGT level of theory, two orbitals are degenerate if the MOs are (a) (anti-)bonding and symmetry related or (b) non-bonding Molecular Orbitals (NBMOs). As the sought degeneracy must occur at the frontier orbitals, we have restricted our exploration to the latter case. In this regard, either HMO or SGT can be employed to evaluate the energy gap between both frontier MOs, ΔE_{ab}, and also to visually assess their non-bonding topology.

Despite Hund's rule predicts a triplet ground state for the degenerate case, further examination of the singly-occupied Molecular Orbitals (SOMOs) topology can be done to anticipate the relative stability of the triplet with respect to the singlet. In this vein, various models for molecular magnetism[2,3] emphasize the linear relationship between ΔE_{ST} and the exchange integral, K_{12}, and its critical importance when both SOMOs are degenerate. The exchange integral is formally defined as the following two-centers two-electrons electron repulsion integral:

$$K_{12} = \int_{-\infty}^{\infty}\int_{-\infty}^{\infty} \frac{\rho(\boldsymbol{r}_1)\rho(\boldsymbol{r}_2)}{|\boldsymbol{r}_2 - \boldsymbol{r}_1|} d\boldsymbol{r}_1 d\boldsymbol{r}_2 \qquad \text{(Eq. 1)}$$

where $\rho(\boldsymbol{r}_i) = \Psi_a(\boldsymbol{r}_i)\Psi_b(\boldsymbol{r}_i)$ corresponds to the overlap density and $\boldsymbol{r}_i$ stands as the coordinates of the *i*-th electron. The exchange integral attains its maximum value when both electrons are close in space, *i.e.*, $|\boldsymbol{r}_i - \boldsymbol{r}_j| \rightarrow 0$. Thus, the magnitude of K_{12} is usually governed by the extrema of the $\rho(\boldsymbol{r}_i)$. Accordingly, diradicals displaying a pair of SOMOs that share significant non-null density regions, while still presenting NBMOs, are prone to present ferromagnetic interactions ($\Delta E_{\mathrm{ST}} > 0$).

Given the specific NBMO topology of the SOMOs considered herein, several approximations can be done to grasp the trends of K_{12} at a low computational cost. First, the SOMOs obtained by means of Hückel MO theory (ψ_1 and ψ_2) are expanded as the usual linear combination of atomic orbitals:

$$\begin{aligned} \psi_1(\boldsymbol{r}) &= \sum\nolimits_i c_{1i}\chi_i(\boldsymbol{r}) \\ \psi_2(\boldsymbol{r}) &= \sum\nolimits_i c_{2i}\chi_i(\boldsymbol{r}) \end{aligned} \qquad \text{(Eq. 2)}$$

where $\psi_i(\boldsymbol{r})$ corresponds to the *i*-th SOMO, $\chi_k(\boldsymbol{r})$ corresponds to the $2p_z$ atomic orbital basis and $\{c_{ik}\}$ is the set of expansion coefficients. Now, as the overlap density is defined as $\rho(\boldsymbol{r}) = \psi_1(\boldsymbol{r})\psi_2(\boldsymbol{r})$, it can be re-expressed as:

$$\rho(\boldsymbol{r}) = \sum_i c_{1i}c_{2i}[\chi_i(\boldsymbol{r})]^2 + 2\sum_i \sum_{j>i} c_{1i}c_{2j}\chi_i(\boldsymbol{r})\,\chi_j(\boldsymbol{r}) \qquad \text{(Eq. 3)}$$

Given the localized nature of the $\chi_k(\boldsymbol{r})$ basis, the products $\chi_k(\boldsymbol{r})\chi_l(\boldsymbol{r}) \to 0$ as the distance between atoms increases or the basis functions become more localized. Assuming a high-localized limit, all the crossed terms vanish, prevailing only the products of basis sets located at the same center. Hence, equation 3 can be approximated as:

$$\rho(\boldsymbol{r}) \approx \sum_i c_{1i}c_{2i}[\chi_i(\boldsymbol{r})]^2 = \sum_i \rho_i(\boldsymbol{r}) \qquad \text{(Eq. 4)}$$

where only the first term of equation 3 remains. Note that, while this approximation would not be valid for slowly-decaying and diffuse atomic orbitals with high principal or azimuthal quantum numbers, the present case study is constrained to the $2p_z$ orbitals of carbon atoms, thus, making this approximation reasonable in this context. In a similar manner, incorporating this approximation into the formal definition of K_{12} (equation 1) results in:

$$K_{12} = \iint \left[\sum_n \frac{\rho_n(\boldsymbol{r}_1)\rho_n(\boldsymbol{r}_2)}{|\boldsymbol{r}_1 - \boldsymbol{r}_2|} + 2\sum_n \sum_{m>n} \frac{\rho_n(\boldsymbol{r}_1)\rho_m(\boldsymbol{r}_2)}{|\boldsymbol{r}_1 - \boldsymbol{r}_2|}\right] d\boldsymbol{r}_1 d\boldsymbol{r}_2 \qquad \text{(Eq. 5)}$$

which, again, can be further simplified as done in equations 3 and 4 for $\rho(\boldsymbol{r})$ as

$$K_{12} \approx \iint \sum_n \frac{\rho_n(\boldsymbol{r}_1)\rho_n(\boldsymbol{r}_2)}{|\boldsymbol{r}_1 - \boldsymbol{r}_2|} d\boldsymbol{r}_1 d\boldsymbol{r}_2 = \sum_n \iint \frac{\rho_n(\boldsymbol{r}_1)\rho_n(\boldsymbol{r}_2)}{|\boldsymbol{r}_1 - \boldsymbol{r}_2|} d\boldsymbol{r}_1 d\boldsymbol{r}_2 \qquad \text{(Eq. 6)}$$

Note that the former expression benefits from the commutation relation between integral and discrete summation operators. Now, recovering the explicit expression for $\rho_i(\boldsymbol{r}) = c_{1i}c_{2i}[\chi_i(\boldsymbol{r})]^2$ utilized in equation 4 it follows that:

$$K_{12} \approx \sum_n (c_{1n}c_{2n})^2 \iint \frac{[\chi_n(\boldsymbol{r}_1)]^2[\chi_n(\boldsymbol{r}_2)]^2}{|\boldsymbol{r}_1 - \boldsymbol{r}_2|} d\boldsymbol{r}_1 d\boldsymbol{r}_2 \qquad \text{(Eq. 7)}$$

Subsequently, noting that $\chi_n(\boldsymbol{r}) = \chi_m(\boldsymbol{r} + \boldsymbol{r}')$, that is, all the orbitals are equivalent except that they are centered at different positions, all the integrals result identical, *i.e.*

$$\tilde{k} \approx \iint \frac{[\chi_n(\boldsymbol{r}_1)]^2[\chi_n(\boldsymbol{r}_2)]^2}{|\boldsymbol{r}_1 - \boldsymbol{r}_2|} d\boldsymbol{r}_1 d\boldsymbol{r}_2 = \iint \frac{[\chi_m(\boldsymbol{r}_1)]^2[\chi_m(\boldsymbol{r}_2)]^2}{|\boldsymbol{r}_1 - \boldsymbol{r}_2|} d\boldsymbol{r}_1 d\boldsymbol{r}_2 \quad \forall\, n, m \qquad \text{(Eq. 8)}$$

where $\tilde{k}$ corresponds to the self-repulsion Coulomb integral. Finally, the expression of K_{12} can be expressed in a compact notation as

$$K_{12} = \tilde{k} \sum_n (c_{1n} c_{2n})^2 \propto \langle \mathbf{c}_1 \circ \mathbf{c}_2 | \mathbf{c}_1 \circ \mathbf{c}_2 \rangle^2 = \mathcal{K}_{12} \qquad \text{(Eq. 9)}$$

where "∘" corresponds to the Hadamard (i.e., point-wise) product.

To elaborate on the implications of the formulation collected in equation 9, consider how it reflects on the (non-)disjoint nature of molecular orbitals. Taking, for instance, a scenario with disjoint SOMOs, any coefficient that is nonzero in ψ_1 is necessarily zero in ψ_2 and *vice versa* by the very definition of disjointness. Consequently, the computation of the pointwise product of their vector coefficients, $\mathbf{c}_1 \circ \mathbf{c}_2$, results in a vector of zeros, thus leading to the conclusion that $\mathcal{K}_{12}$ is zero and confirms the disjoint character of the SOMOs. Conversely, when considering non-disjoint SOMOs, some coefficients that are nonzero in ψ_1 are also nonzero in ψ_2. In this case, the pointwise product $\mathbf{c}_1 \circ \mathbf{c}_2$ must also have non-zero elements in agreement with a significant overlap density. The magnitude of $\mathcal{K}_{12}$, thus, serves as a rough indicator of the degree of non-disjointness between the SOMOs.

We employed this theoretical framework to pre-screen the non-bonding molecular orbitals (NBMOs) and non-disjoint character of all pentalene-like molecules explored in this work. Due to the simplicity of the method, the execution time for a moderately sized molecule is lower than the order of a second. Moreover, despite the evident limitations of this approach, our *Ab Initio* results and conclusions interestingly correlate well with such a simplistic procedure, showcasing its utility in the preliminary analysis of open-shell character in planar fully-conjugated systems. On a lesser note, SGT is unable to differentiate between the effect of different types of atoms in the set up defined so far. In this regard, the method is limited to all-carbon systems. However, if the incorporation of a hetero-atom does not significantly alter the MO topology, the SGT approach can still provide correct trends.

S2. Spectral Graph Theory Results

In the following section the molecular orbital representation of the diradicals derived from **DPA[*n*]**, and **DBP** are shown. As SGT method is not able to differentiate between hetero-substitutions only the full-carbon scaffolds are considered here.

S2.1. MO topology of the structural isomers of My$_2$-DPA[0]

Figure S1 shows the frontier orbitals for all the possible structural isomers of **My$_2$-DPA[0]**. Among them, only **2,5-My$_2$-DPA[0]** has a set of two nonbonding frontier orbitals. Accordingly, **2,5-My$_2$-DPA[0]** is the only isomer displaying degenerate SOMOs and, thus, it is the only structural isomer for which a significant ΔE_{ST} gap can be predicted.

Interestingly, different scenarios are found across the rest of the isomers. For example, the frontier orbitals of **1,2-**, **1,4-**, and **2,4-My$_2$-DPA[0]** compounds have both bonding and anti-bonding character, while for **1,3-** and **1,6-My$_2$-DPA[0]** one of the MOs features a non-bonding character (see MO$_a$). This diversity illustrates the key importance of atomic connectivity in designing diradicals with specific properties. Note that, although not shown here, the results presented hereafter for **DPA[0]** couplers extend to the whole **DPA[*n*]** series.

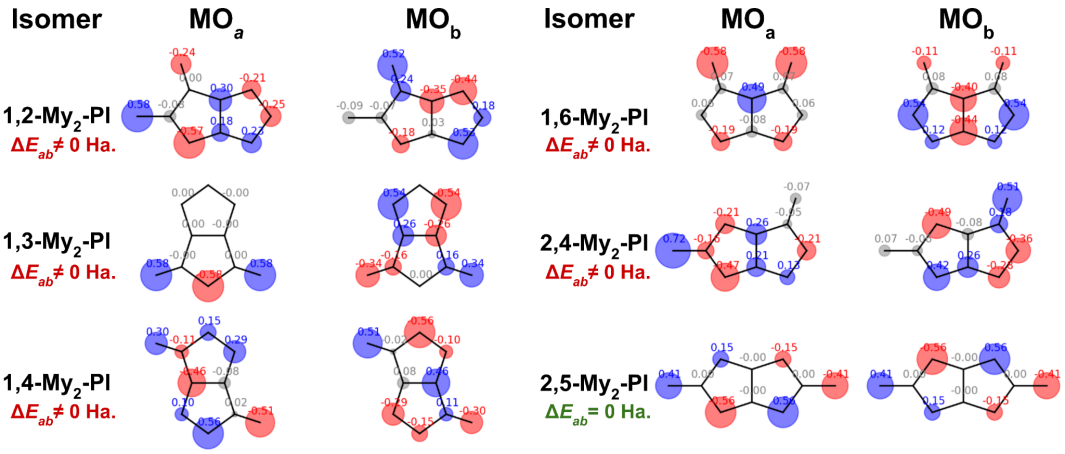

Figure S1. SOMOs topology and ΔE_{ab} (gap between SOMOs 'a' and 'b') for all the structural isomers of My$_2$-DPA[0]. While all the compounds are found to possess a pair of non-disjoint SOMOs, the only isomer displaying a gap of ΔE_{ab} = 0 is 2,5-My$_2$-DPA[0]. Note that **Pl** stands for **DPA[0]** in the main text.

S2.2. My$_2$-DPA[*n*] singly-occupied Molecular Orbitals (SOMOs)

The energy diagram of the π-electron system for **My$_2$-DPA[0]** and **My$_2$-DPA[3]**, which are the lowest and highest order dicyclopenta-[*n*]acene considered in this work, are shown in Figure S2a and S2b.

As illustrated, the SOMOs of both compounds are predicted degenerate at SGT level (see levels highlighted in red). Moreover, the pair of SOMOs comprise a non-disjoint set (see Figure S2), specially displaying a significant non-null overlap density on the **My** carbon atoms, thus anticipating a positive ΔE_{ST} gap in both cases. The SGT-based SOMOs for all compounds of the **My$_2$-DPA[*n*]** series present similar MO topology. However, as illustrated in Figure S2c, we have observed a decrease in K_{12} as increasing the acene size (n), possibly attributed to the higher delocalization of the SOMOs as progressing through the series. Accordingly, the SGT results indicate a lower ΔE_{ST} gap for larger values of n.

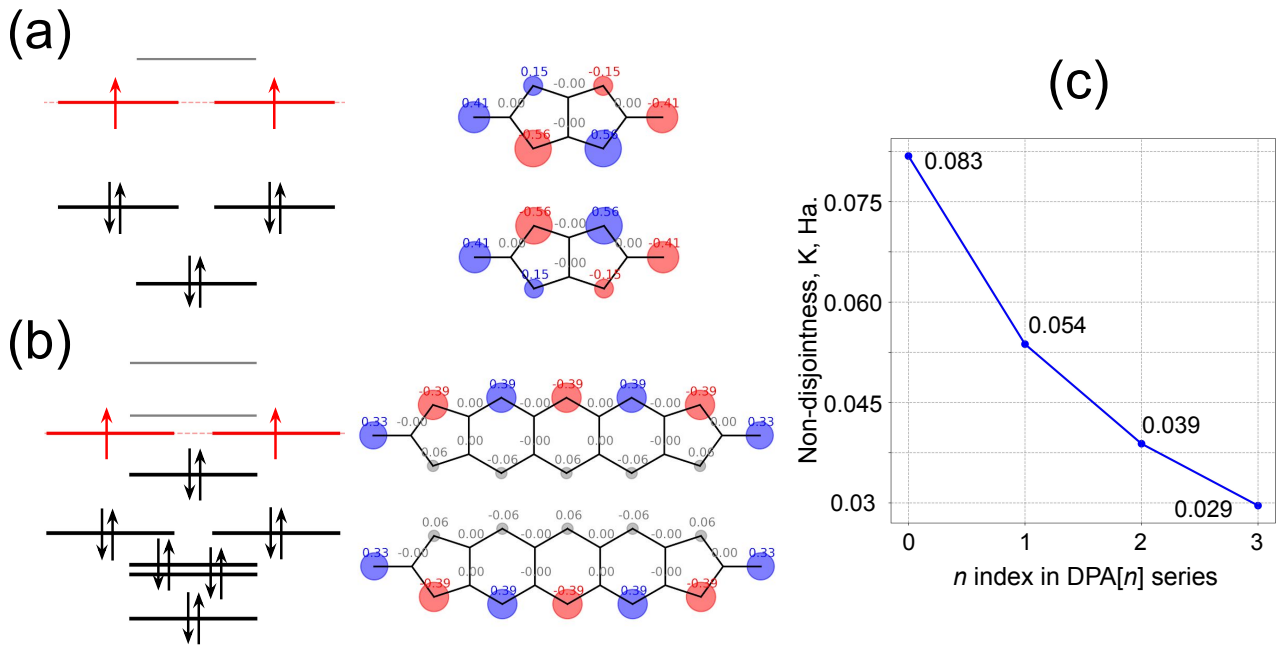

Figure S2. Schematic representation of SGT results for My$_2$-DPA[n] series. The energy levels of the π-system, occupation, and the most non-disjoint linear combination of SOMO projected onto the carbon scaffold for (a) My$_2$-DPA[0] and (b) My$_2$-DPA[3] compounds are shown. For the pair of two most non-disjoint SOMOs, see inset coefficients of the corresponding linear combination. (c) Approximate exchange integral (K), computed as explained in Section S1, for the first 4 (n=0,3) **My$_2$-DPA[*n*]** diradicals.

S2.3. My$_2$-DBP singly-occupied Molecular Orbitals (SOMOs)

Figure S3 shows the summary of SGT results for the different structural isomers of **My$_2$-DBP** diradicals. We have observed a non-disjoint set of MOs in all the cases (see MOs in the first and second columns and the overlap density at the third one), thus leading to a substantial overlap density and K_{12} in all the cases. Moreover, a degenerate pair of SOMOs is predicted for **2,7-** and **4,9-My$_2$-DBP** diradicals (see Figure S3b,d) and, thus, a substantial ΔE_{ST} gap can be anticipated in both cases. Our results show, however, that **1,6-** and **3,8-My$_2$-DBP** compounds possess non-degenerate MOs (see

Figure S3a,c) and, thus, a negative ΔE_{ST} gap is predicted in these cases. Bearing in mind the substantial value of K_{12}, more accurate calculations must be carried out to determine the spin alignment of the ground state.

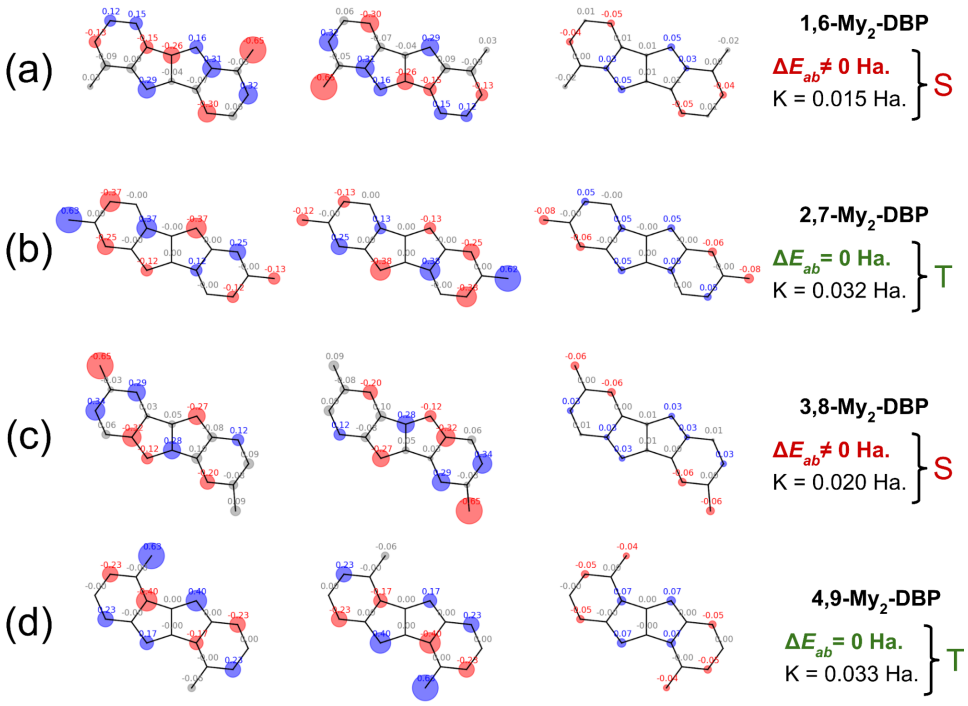

Figure S3. SOMOs topology, overlap density and ΔE_{ab} (gap between maximally disjoint SOMOs) for all the structural isomers of My_2-DBP. While all the compounds are found to possess a pair of non-disjoint SOMOs, the only isomers displaying a gap of ΔE_{ab} = 0 are **2,7-My_2-DBP** and **4,9-My_2-DBP**.

S3. Mulliken spin population and ERIs

In the following section, the Mulliken spin population and some relevant molecular orbital integrals for the gap are shown. The population analysis has been obtained straightforwardly from the output of the optimization calculations using Gaussian09 package. However, Gaussian09 package does not provide a ready-to-use access to Coulomb, Exchange or other two-electron repulsion integrals (ERIs) at the MO basis. For this reason, the MO integrals have been evaluated separately in pySCF, using the atomic positions of the ground state of each diradical as obtained from PBE0/6-311G* in Gaussian09. Note we employed the same PBE0/6-311G* level of theory for pySCF calculations.

S3.1. Mulliken spin population of My_2-DPA[*n*] and My_2-DADPA[*n*] diradicals

Figure S4 shows the Mulliken spin population (MSP) of **My_2-DPA[*n*]** and **My_2-DADPA[*n*]** diradicals at the triplet (*S*=1) and singlet (*S*=0) spin multiplicities. Overall, we found that the spin distribution at a given *n* is substantially different for *S*=0 and *S*=1 (see positive and negative MSP distribution colored in purple and yellow, respectively). Particularly, for the **My_2-DPA[*n*]** series, we found that the MSP distribution at *S*=0 at the **My** cores and its adjacent atoms is null. However, for *S*=1, the carbon atom of the **My** core possesses a large spin population. Overall, the MSP analyses indicate that unpaired electrons are substantially more delocalized in the triplet than in the singlet spin configuration. Although the **My** core displays a non-null MSP for singlet in the **My_2-DADPA[*n*]** series, its magnitude is considerably lower compared to the triplet state.

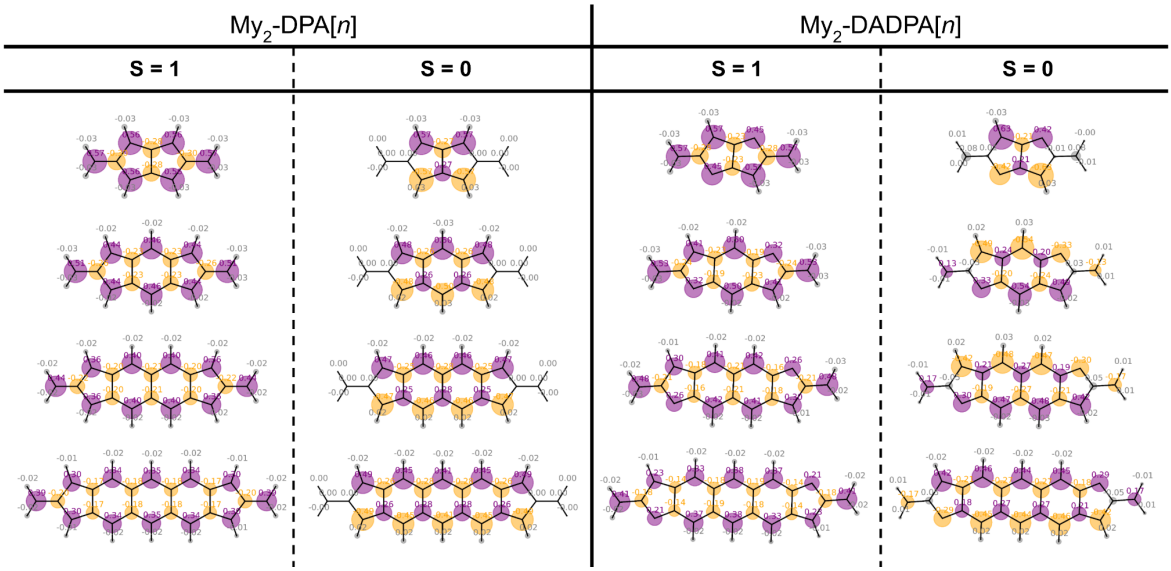

Figure S4. Atom-resolved Mulliken spin population (MSP) for **My_2-DPA[n]** and **My_2-DADPA[n]**. First and second columns correspond to *S*=1 and *S*=0 spin multiplicities for **My_2-DPA[n]** while third and fourth columns correspond to **My_2-DADPA[n]**. Positive and negative populations are indicated in purple and yellow, respectively. The marker size is in agreement with its magnitude.

S3.2. ERIs of My$_2$-DPA[*n*] and My$_2$-DADPA[*n*] diradicals

Figure S5 illustrates exchange (K_{12}), Coulomb self-repulsion (J_{11}) and Coulomb inter-repulsion (J_{12}) electron repulsion integrals (ERIs) along the **My$_2$-DPA[*n*]** and **My$_2$-DADPA[*n*]** series (colored in blue and red, respectively). We have observed that all the ERIs decrease as the [*n*]acene size increases. The trend is related to the increasing delocalization of the SOMOs as *n* increases. That is, for high values of *n*, the exchange integral, K_{12}, is lower than for smaller *n*'s and, thus, the ΔE_{ST} gap decreases as *n* increases. Our results also determine a larger slope for **My$_2$-DADPA[*n*]** than for **My$_2$-DPA[*n*]** series, in agreement with the slope registered for the corresponding ΔE_{ST} gaps, reported in the main text.

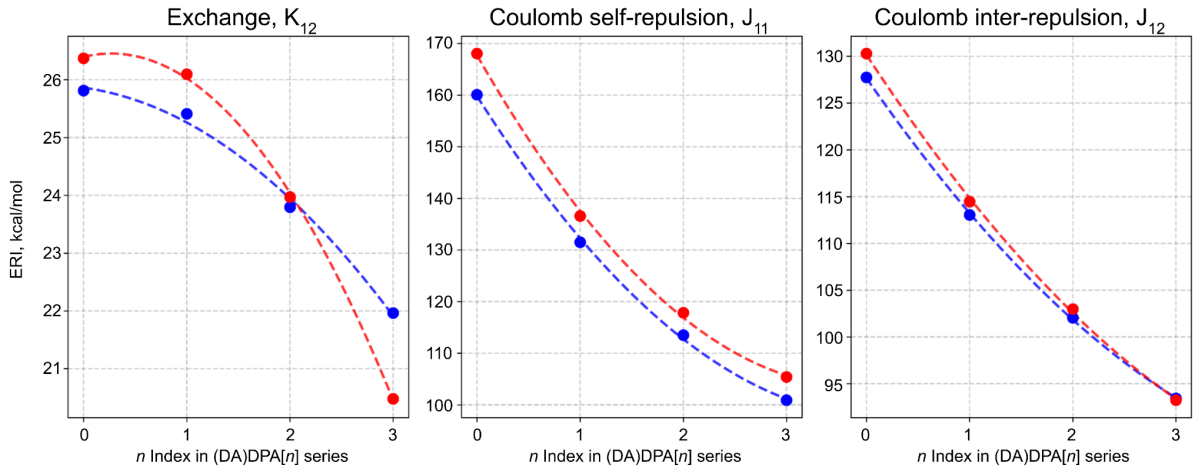

Figure S5. Electron Repulsion Integrals (ERIs) for **My$_2$-DPA[*n*]** and **My$_2$-DADPA[*n*]** series, colored in blue and red, respectively. Dashed lines do not indicate continuity, instead, these are only included as a guide to the eye. The ERI type is documented on top of each plot.

S3.3. Spin population of My$_2$-(DA)DPA[*n*] and DPM$_2$-(DA)DPA[*n*]

Figure S6 illustrates the Mulliken spin population (MSP) for **My** and **DPM** cores. In agreement with the ΔE_{ST} gap results, we have only observed a small effect of the core's choice to the MSP in both *S*=0 and *S*=1 spin multiplicities. MSP results indicate that the **DPM** core does not critically quench the spin distribution and, thus, neither does it affect the ΔE_{ST} gap.

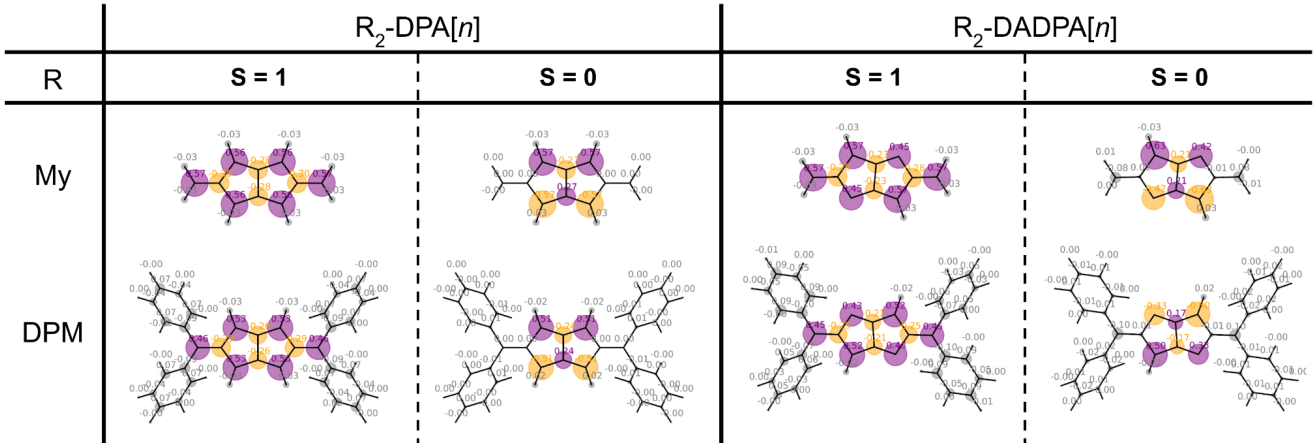

Figure S6. Atom-resolved Mulliken spin population (MSP) for **R_2-DPA[0]** and **R_2-DADPA[0]**. First and second columns correspond to *S*=1 and *S*=0 spin multiplicities for **R_2-DPA**[**0**] while third and fourth columns correspond to **R_2-DADPA**[**0**]. First and second columns correspond to **R=My** and **R=DPM** cores. Positive and negative populations are indicated in purple and yellow, respectively. The marker size is in agreement with its magnitude.

S3.4. Mulliken spin population of R_2-DBP and R_2-DADBP diradicals

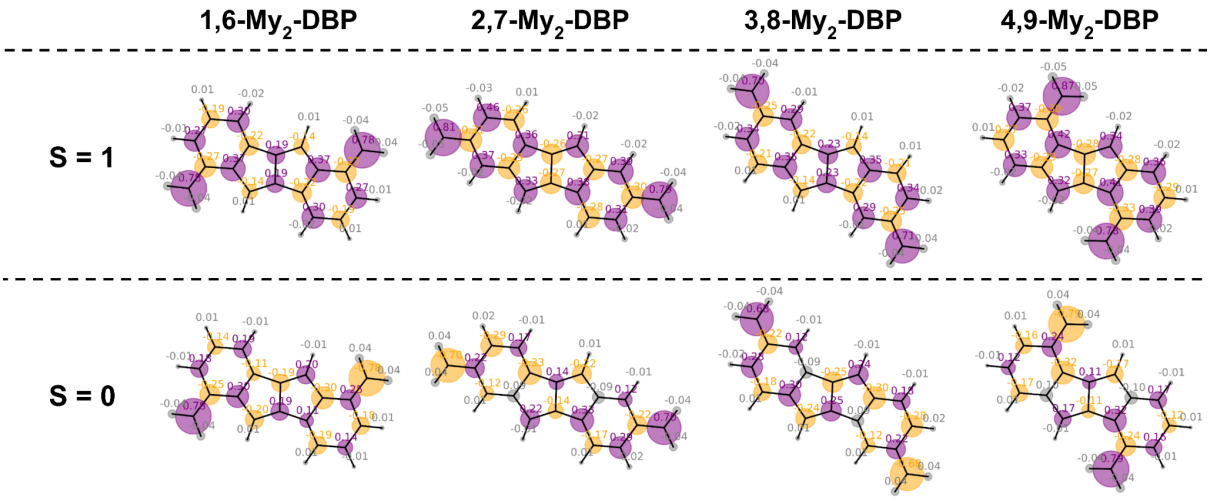

Figure S7. Mulliken spin population (MSP) for various **My_2-DBP** structural isomers. First and second rows correspond to *S*=1 and *S*=0 spin multiplicities. Positive and negative populations are indicated in purple and yellow, respectively. The marker size is in agreement with the magnitude of the MSP.

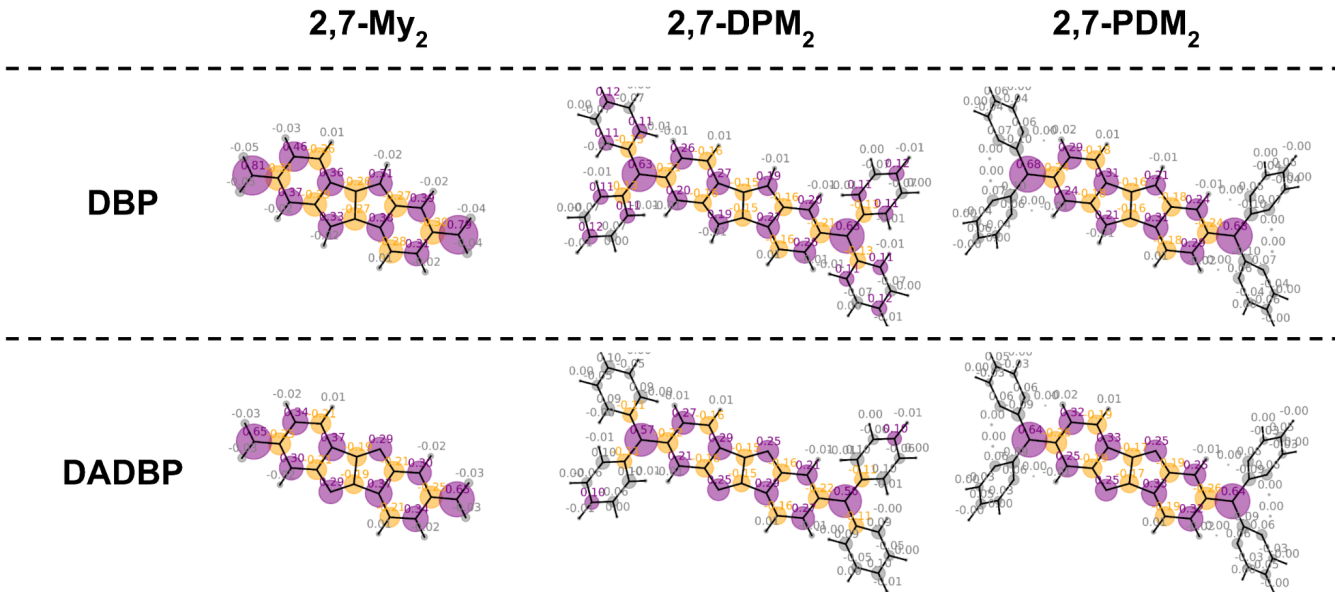

Figure S8. Mulliken spin population (MSP) for different core substitutions (**R=My, DPM, PDM**) of **2,7-R$_2$-DBP**. First and second rows correspond to *S*=1 and *S*=0 spin multiplicities. Positive and negative populations are indicated in purple and yellow, respectively. The marker size is in agreement with the magnitude of the MSP.

S4. Further results related to ΔE_{ST} gaps

S4.1. B3LYP and LC-ω-PBE ΔE_{ST} gaps

Table S1. Comparison of ΔE_{ST} gaps (in kcal/mol) obtained for **My$_2$-DPA[*n*]** and **My$_2$-DADPA[*n*]** using different exchange correlation functionals. Note the good agreement between PBE0 and B3LYP (and thus with DDCI) and the overestimation of the LC-ω-PBE functional.

Radical/Method	PBE0	B3LYP	LC-ω-PBE
My$_2$-DPA[0]	7.1	5.8	10.3
My$_2$-DPA[1]	2.3	1.6	3.3
My$_2$-DPA[2]	-2.7	-2.2	-7.6
My$_2$-DPA[3]	-7.2	-5.5	-17.8
My$_2$-DADPA[0]	8.0	6.6	11.1
My$_2$-DADPA[1]	4.6	3.9	5.8
My$_2$-DADPA[2]	1.1	1.0	-2.9
My$_2$-DADPA[3]	-3.0	-2.0	-10.9

S4.2. CAS(10,10) Active MOs and Multi-referential CASSCF weights

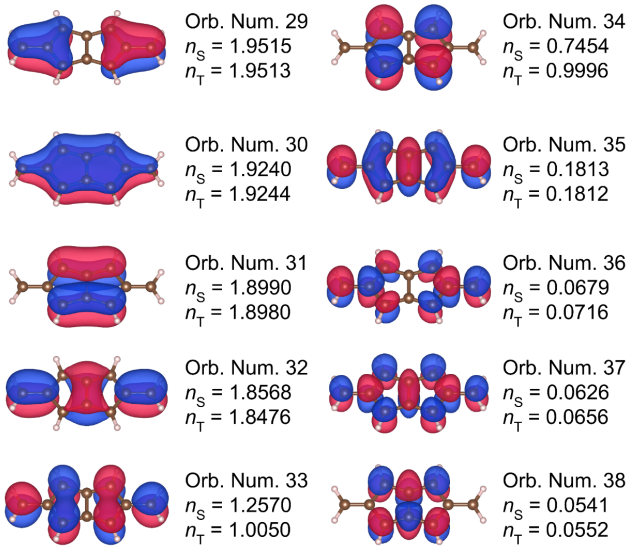

S = 0

N°	W	0.50	0.26	0.05	0.02	–
	36	–	–	–	–	–
	35	–	–	↓	–	–
	34	–	↑↓	↑	–	–
	33	↑↓	–	↓	–	–
	32	↑↓	↑↓	↑	–	–
	31	↑↓	↑↓	↑↓	–	–

S = 1

N°	W	0.75	0.05	0.02	0.02	–
	36	–	–	–	–	–
	35	–	↓	↓	↑↓	–
	34	↑	↑	↑	↑	–
	33	↑	↑	↑	↑	–
	32	↑↓	↑	↑↓	–	–
	31	↑↓	↑↓	↑	↑↓	–

Figure S9. Left: Molecular orbitals of the active space of the CAS(10,10) calculation of **My$_2$-DPA[0]**. The occupation number for each orbital in both the singlet (n_S) and triplet (n_T) states is reported. Right: Scheme of the most important configurations contributing to the total CASSCF wavefunction (w denotes the weight of each configuration).

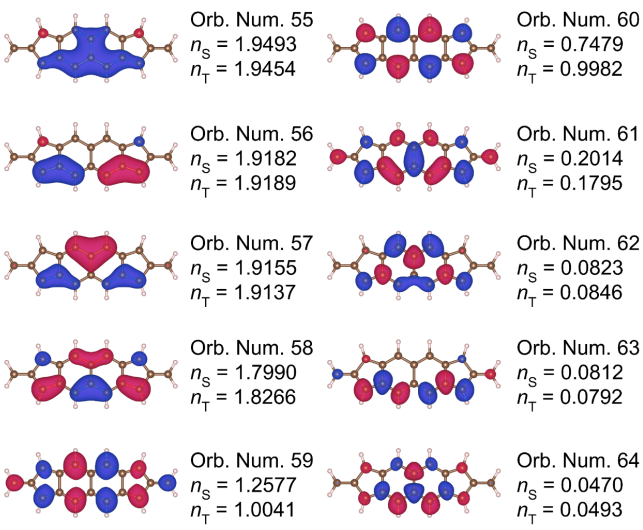

S = 0						
	W	0.48	0.25	0.08	0.02	0.01
N°	62	–	–	–	↓	–
	61	–	–	↓	–	–
	60	–	↑↓	↓	↓	↓
	59	↑↓	–	↑	↑	↑
	58	↑↓	↑↓	↑	↑↓	↑↓
	57	↑↓	↑↓	↑↓	↑	↑↓

S = 1						
	W	0.74	0.02	0.02	0.02	0.01
N°	62	–	–	–	–	–
	61	–	↓	↓	↓	↑↓
	60	↑	↑	–	↑↓	↑
	59	↑	↑	↑↓	–	↑
	58	↑↓	↑	↑	↑	–
	57	↑↓	↑↓	↑↓	↑↓	↑↓

Figure S10. Left: Molecular orbitals of the active space of the CAS(10,10) calculation of **My$_2$-DPA[2]**. The occupation number for each orbital in both the singlet (n_S) and triplet (n_T) states is reported. Right: Scheme of the most important configurations contributing to the total CASSCF wavefunction (w denotes the weight of each configuration).

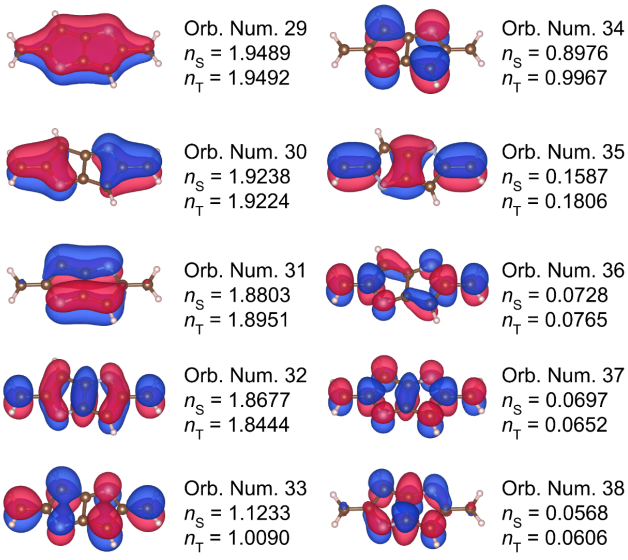

S = 0						
	W	0.43	0.33	0.04	0.01	–
N°	36	–	–	–	↑↓	–
	35	–	–	↓	–	–
	34	–	↑↓	↑	↑↓	–
	33	↑↓	–	↓	↑↓	–
	32	↑↓	↑↓	↑	↑↓	–
	31	↑↓	↑↓	↑↓	–	–

S = 1						
	W	0.74	0.06	0.02	0.02	–
N°	36	–	–	–	↑	–
	35	–	↓	↓	–	–
	34	↑	↑	↑	↑	–
	33	↑	↑	↑	↑	–
	32	↑↓	↑	↑↓	↓	–
	31	↑↓	↑↓	↑	↑↓	–

Figure S11. Left: Molecular orbitals of the active space of the CAS(10,10) calculation of **My$_2$-DADPA[0]**. The occupation number for each orbital in both the singlet (n_S) and triplet (n_T) states is reported. Right: Scheme of the most important configurations contributing to the total CASSCF wavefunction (w denotes the weight of each configuration).

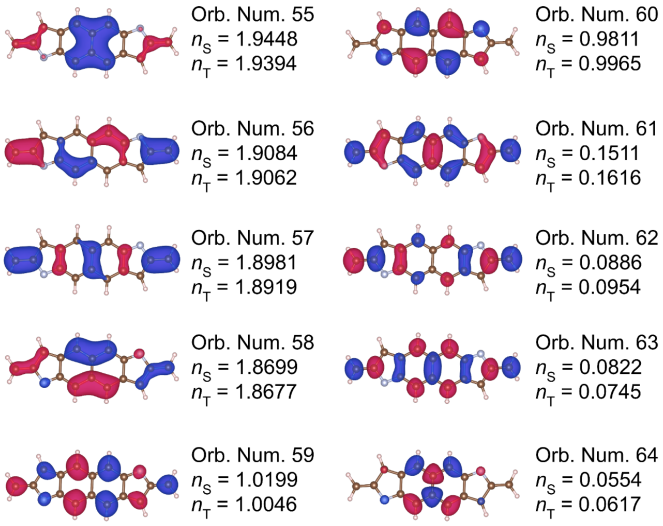

S = 0

	W	0.39	0.37	0.05	0.01	–
N°	62	–	–	–	–	–
	61	–	–	↓	↓	–
	60	–	↑↓	↑	–	–
	59	↑↓	–	↓	↑	–
	58	↑↓	↑↓	↑	↑	–
	57	↑↓	↑↓	↑↓	↑↓	–

S = 1

	W	0.75	0.02	0.09	0.09	0.09
N°	62	–	↓	–	↓	–
	61	–	↑	↓	–	↑↓
	60	↑	↑	–	↑	↑
	59	↑	↑	↑↓	↑	↑
	58	↑↓	↑↓	↑↓	↑↓	–
	57	↑↓	↑↓	↑	↑	↑↓

Figure S12. Left: Molecular orbitals of the active space of the CAS(10,10) calculation of My$_2$-DADPA[2]. The occupation number for each orbital in both the singlet (n_S) and triplet (n_T) states is reported. Right: Scheme of the most important configurations contributing to the total CASSCF wavefunction (w denotes the weight of each configuration).

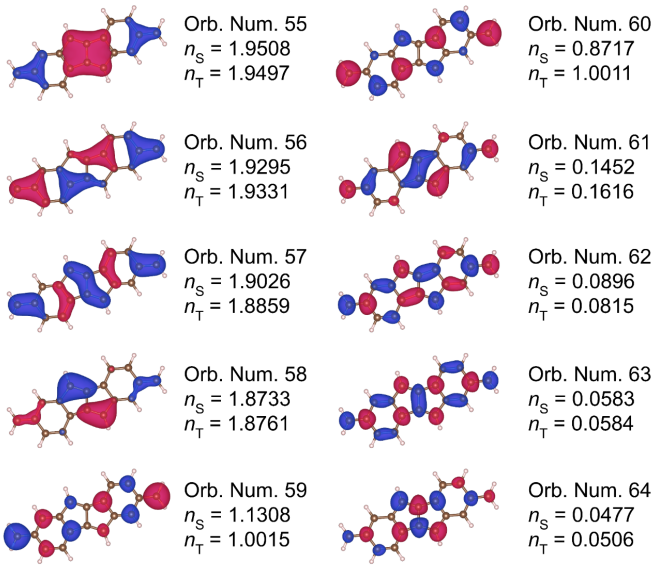

S = 0

	W	0.45	0.33	0.03	0.02	0.01
N°	62	–	–	↓	–	–
	61	–	–	–	↑	↑↓
	60	–	↑↓	↑	↓	–
	59	↑↓	–	↓	↑	↑↓
	58	↑↓	↑↓	–	↓	–
	57	↑↓	↑↓	↑	↑↓	↑↓

S = 1

	W	0.77	0.04	0.01	0.01	–
N°	62	–	–	–	↓	–
	61	–	↓	↑↓	↑	–
	60	↑	↑	↑	↑	–
	59	↑	↑	↑	↑	–
	58	↑↓	↑	↑↓	↓	–
	57	↑↓	↑↓	–	↑	–

Figure S13. Left: Molecular orbitals of the active space of the CAS(10,10) calculation of **2,7-My$_2$-DBP**. The occupation number for each orbital in both the singlet (n_S) and triplet (n_T) states is reported. Right: Scheme of the most important configurations contributing to the total CASSCF wavefunction (w denotes the weight of each configuration).

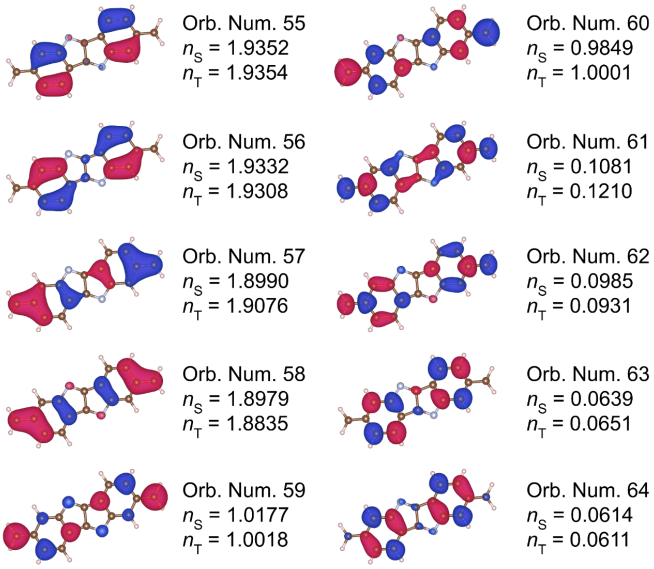

S = 0

	W	0.39	0.38	0.05	0.05	–
N°	62	–	–	–	↑	–
	61	–	–	↑	↑↓	–
	60	–	↑↓	↑	↓	–
	59	↑↓	–	↓	↑	–
	58	↑↓	↑↓	↓	↑↓	–
	57	↑↓	↑↓	↑↓	↓	–

S = 1

	W	0.77	0.04	0.02	0.01	–
N°	62	–	–	↓	↓	–
	61	–	↓	–	↑	–
	60	↑	↑	↑	↑	–
	59	↑	↑	↑	↑	–
	58	↑↓	↑	↑↓	↓	–
	57	↑↓	↑↓	↑	↑	–

Figure S14. Left: Molecular orbitals of the active space of the CAS(10,10) calculation of 2,7-My$_2$-DADBP. The occupation number for each orbital in both the singlet (n_S) and triplet (n_T) states is reported. Right: Scheme of the most important configurations contributing to the total CASSCF wavefunction (w denotes the weight of each configuration).

S4.3. Convergence of the DDCI parameters

Table S2. Values of ΔE_{ST} using different values for TSel and TPre parameters in the DDCI calculations of **My$_2$-DPA[0]**. The selected TPre and TSel values for the rest of the DDCI calculations performed along this work are given in bold.

Method/Radical	**Parameter**					
TPre	10^{-4} (*default*)	**10^{-4}**	10^{-4}	10^{-4}	10^{-5}	10^{-6}
TSel	10^{-6} (*default*)	**10^{-10}**	10^{-11}	10^{-9}	10^{-10}	10^{-10}
ΔE_{ST} (cm^{-1})	2628.7	**2546.1**	2546.2	2545.7	2546.1	2546.1

Table S3. Comparison of singlet-triplet energy gaps (ΔE_{ST} in kcal/mol) for **2,7-My$_2$-DBP** and **2,7-My$_2$-DADBP** calculated using DFT/PBE0, DDCI(4,4) and CASSCF, using active spaces of increasing size (2,2) to (10,10).

Method/Radical	**2,7-My$_2$-DBP**	**2,7-My$_2$-DADBP**
DFT/PBE0	3.46	5.06
DDCI(4,4)	2.75	-
CAS(2,2)	0.13	0.34
CAS(4,4)	6.84	8.27
CAS(10,10)	1.30	2.59

S4.4. Lewis Structures of My_2-DBP

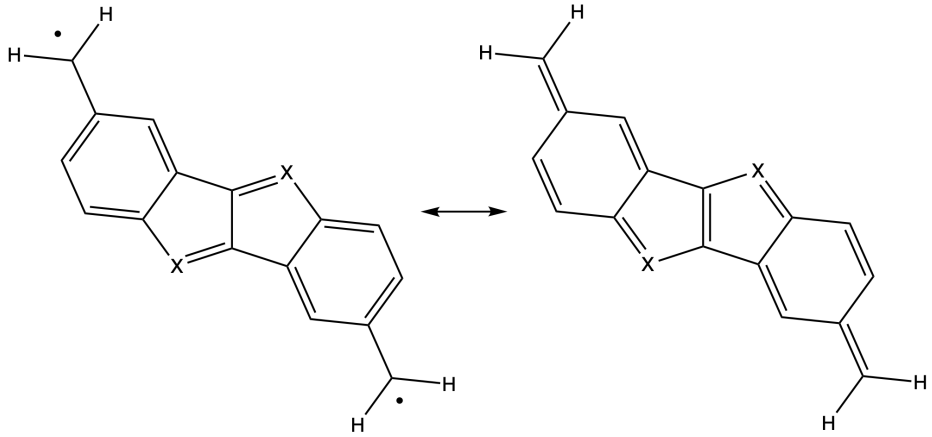

Figure S15. Representative Lewis structures of **3,8-My_2-DBP** diradical. Note the closed-shell character of the Lewis structure on the right.

S5. Further Stability Results

S5.1. Bond Length Alternation Results

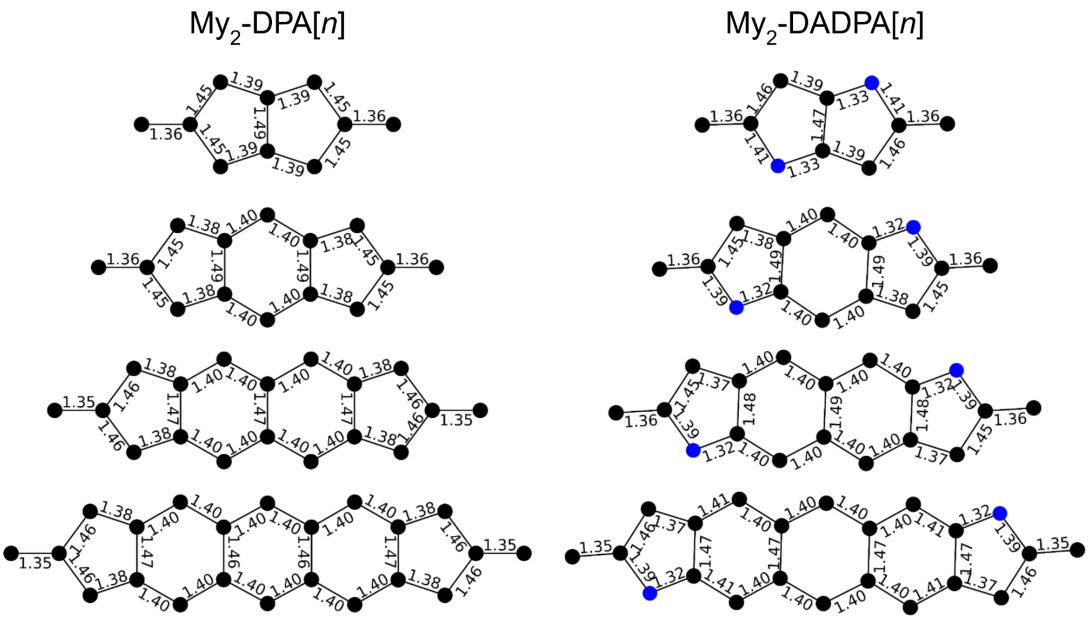

Figure S16. BLA across the **My$_2$-DPA[*n*]** and **My$_2$-DADPA[*n*]** series (with *n*=0–3).

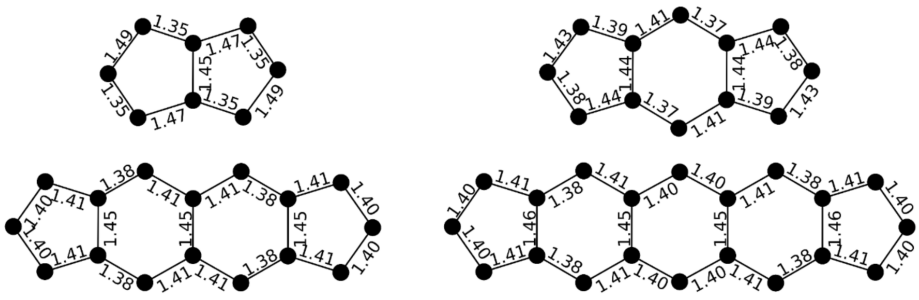

Figure S17. BLA across the bare **DPA[*n*]** series (with *n*=0–3).

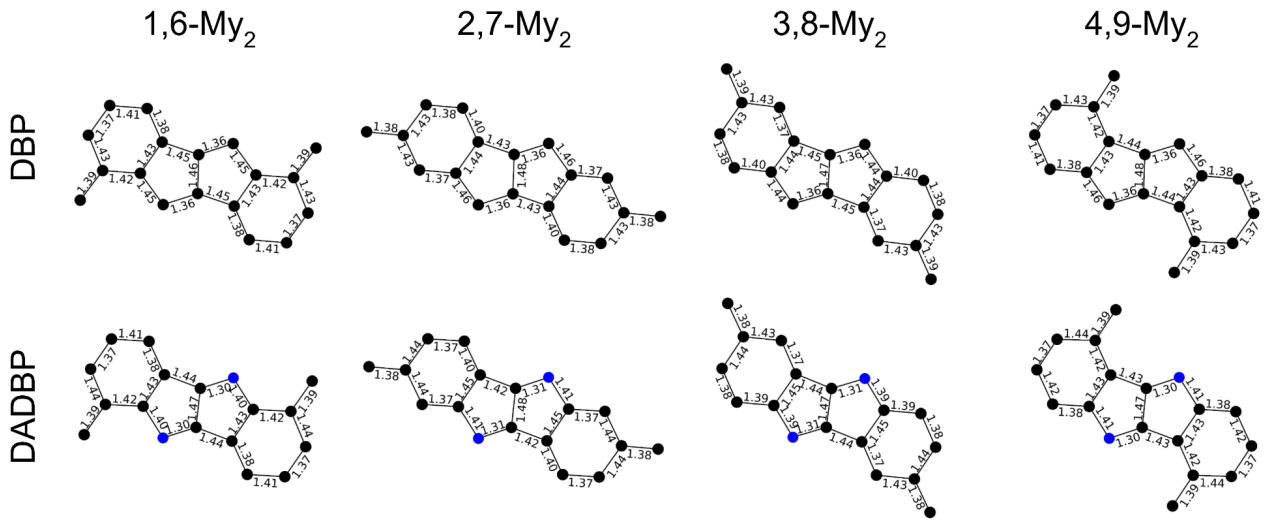

Figure S18. BLA of the different constitutional isomers of **My$_2$-DBP** and **My$_2$-DADBP**.

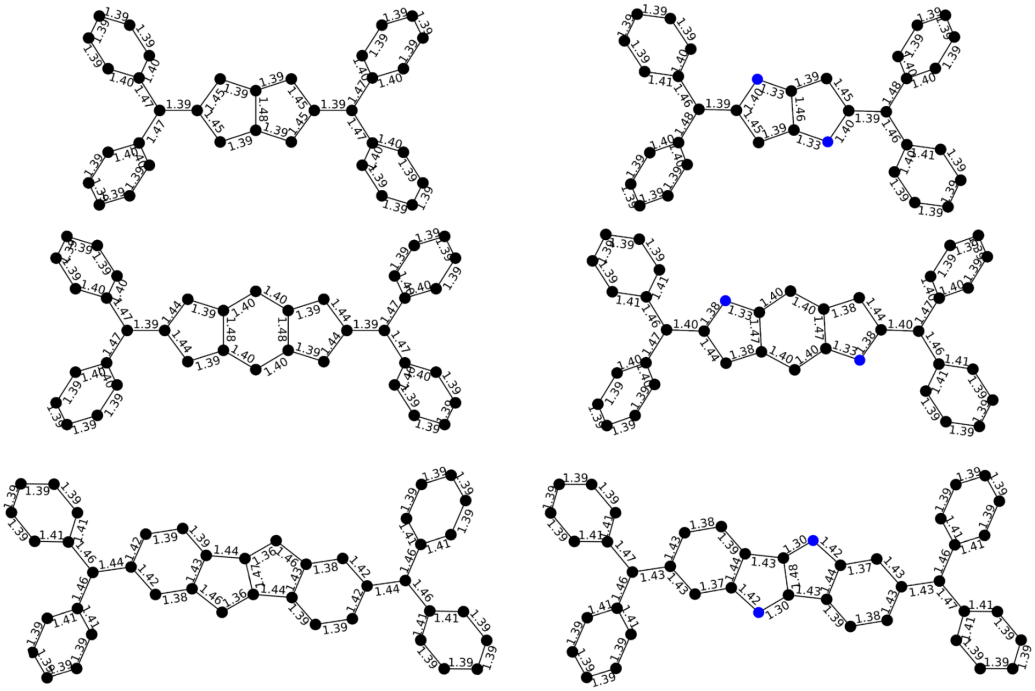

Figure S19. BLA of the DPM-substituted diradicals with the largest positive ΔE_{ST} gap. Left: **DPM$_2$-DPA[0]**, **DPM$_2$-DPA[1]** and **2,7-DPM$_2$-DBP**. Right: **DPM$_2$-DADPA[0]**, **DPM$_2$-DADPA[1]** and **2,7-DPM$_2$-DADBP**.

S5.2. Further NICS results for My$_2$-DADPA[*n*] series

In the diaza-series, *i.e.* **My$_2$-DADPA[*n*]**, a systematic reduction in NICS$_{ZZ}$(1) is generally observed in comparison to their all-carbon analogs (for instance, see in Figure 4a of the main text how 0.3 ppm in **My$_2$-DPA[0]** at OSS becomes -3.2 ppm when **My$_2$-DADPA[0]** is considered). This reduction may be attributed to the incorporation of nitrogen atoms into the molecular scaffold, which potentially allows for C=N imine interactions. Moreover, the presence of nitrogen atoms could enhance the electron density in the π-system, shifting the 4*n* electronic configuration towards a 4*n*+2 configuration. Notably, the difference in NICS$_{ZZ}$(1) values between the bare units and their diradical derivatives is more pronounced in the diaza series rather than in the all-carbon analogs. This could suggest an increased propensity of **My$_2$-DADPA[*n*]** series to form diradicals.

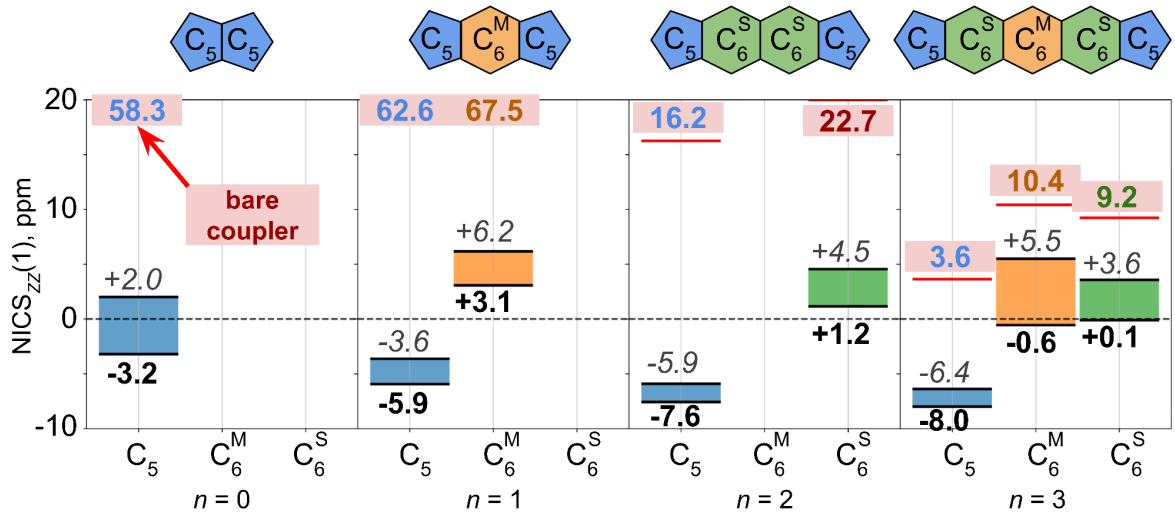

Figure S20. NICS$_{ZZ}$(1) values for the constituent rings (C_5, C_6^M, and C_6^S) of **My$_2$-DADPA[*n*]** diradicals across the total number of fused [*n*]acenes (i.e., *n* in x-axis). NICS$_{ZZ}$(1) values are given for both triplet (T, italic) and singlet (OSS, bold) states. The NICS$_{ZZ}$(1) gaps are given using the following color code: blue (C_5), orange (C_6^M), and green (C_6^S). The values for bare couplers are framed in red for each ring.

S5.3. Further NICS results for My_2-DBP isomers

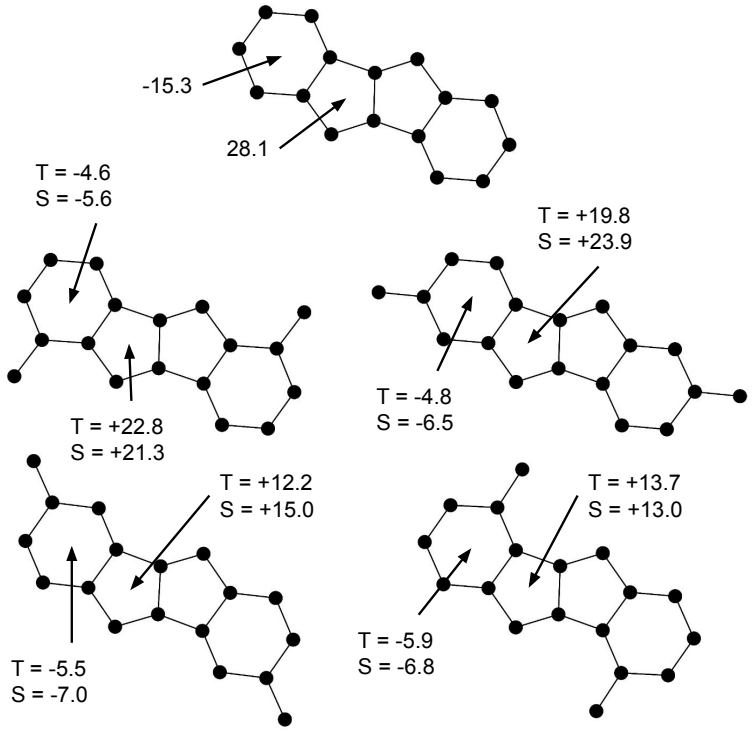

Figure S21. $NICS_{ZZ}(1)$ values in ppm for the different constitutional isomers of **My_2-DBP**. The $NICS_{ZZ}(1)$ values are provided for both the triplet (T) and singlet (S) states.

S6. Structure of the data collected in the Repository

/calcs/: Root folder for all the calculations.

- **01_Delta_ST/**: (Main folder of ΔE_{ST} gaps calculations with PBE0, *i.e.*, the main functional reported. All calculations are in G09 format, providing both the input and output).
  - **01_R2-DPA/**: **R_2-DPA[*n*]** calculations.
    - **01_My/**: Main folder for **R=My**.
      - **n_0/**: **My_2-DPA[0]** (Code: GO: Geometry Optimization, SP: Single Point, T: Triplet state, S: Singlet state.)
        - GO_S.dat & GO_S.log
        - GO_T.dat & GO_T.log
        - SP_S.dat & SP_S.log
        - SP_T.dat & SP_T.log
      - **n_1/**: Same files as in **n_0**.
      - **n_2/**: Same files as in **n_0**.
      - **n_3/**: Same files as in **n_0**.
    - **02_DPM/**: Main folder for **R=DPM**. The sub-folder structure is similar to **01_My**.
    - **03_PDM/**: Main folder for **R=PDM**. The sub-folder structure is similar to **01_My**.
  - **02_R2-DADPA/**: Analogous diradicals derived from diaza-derivatives. The sub-folder structure is similar to the one of **01_R2-DPA**.
  - **03_R2-DBP/**: **R_2-DBP** calculations.
    - **01_My/**:
      - **1_6_isomer/**:
        - GO_S.dat & GO_S.log
        - GO_T.dat & GO_T.log
        - SP_S.dat & SP_S.log
        - SP_T.dat & SP_T.log
      - **2_7_isomer/**: Same files as in **1_6_isomer**.
      - **3_8_isomer/**: Same files as in **1_6_isomer**.
      - **4_9_isomer/**: Same files as in **1_6_isomer**.
    - **02_DPM/**: Main folder for **R=DPM**. The sub-folder structure is similar to **01_My**.
    - **03_PDM/**: Main folder for **R=PDM**. The sub-folder structure is similar to **01_My**.

- **04_R2-DADBP/**: Analogous diradicals derived from diaza-derivatives. The sub-folder structure is similar to the one of **01_R2-DPA**.

- **02_Protected_Couplers/**: ΔE_{ST} gaps for **R_2-(DA)DPA[1]** diradicals.
  - **01_R2-DPA/**: Substituted **R_2-DPA[1]** calculations.
    - **01_My/**: Main folder for R=My.
      - **01_NH2/**:
        - GO_S.dat & GO_S.log
        - GO_T.dat & GO_T.log
        - SP_S.dat & SP_S.log
        - SP_T.dat & SP_T.log
      - **02_NMe2/**: Similar files as in **01_NH2/**.
      - **03_NO2/**: Similar files as in **01_NH2/**.
      - **04_CN/**: Similar files as in **01_NH2/**.
      - **05_MESITYL/**: Similar files as in **01_NH2/**.
    - **02_DPM/**: Main folder for **R=DPM**. Similar folder structure as in **01_NH2/**.
    - **03_PDM/**: Main folder for **R=PDM**. Similar folder structure as in **01_NH2/**.
  - **02_R2_DADPA/**: Substituted **R_2-DADPA[1]**. Similar folder structure as in **01_R2-DPA/**.

- **03_NICS/**: All the NICS calculations.
  - **01_ring_centers/**:
    - **01_My2-DPA/**:
      - **01_precursors/**:
        - **n_0/**
        - **n_1/**: Same files as in **n_0**.
        - **n_2/**: Same files as in **n_0**.
        - **n_3/**: Same files as in **n_0**.
      - **02_diradicals/**: Similar structure as in **01_precursors**.
    - **02_My2-DADPA/**: Similar structure as in **01_My2-DPA**.
    - **03_My2-DBP/**:
      - **01_precursors/**:
        - **1_6_isomer/**
        - **2_7_isomer/**: Same files as in **1_6_isomer**.
        - **3_8_isomer/**: Same files as in **1_6_isomer**.
        - **4_9_isomer/**: Same files as in **1_6_isomer**.

        - **02_diradicals/**: Similar structure as in **01_precursors**.
    - **04_My2-DADBP/**: Similar structure as in **01_My2-DPA**.
- **02_surf_iso/**:
    - **01_My2-DPA_0/**:
        - **01_precursor/**:
        - **02_diradical/**:
    - **02_My2-DBP_2_7_isomer/**:
        - **01_precursor/**:
        - **02_diradical/**:

References

[1] C. A. Coulson, B. O'Leary, R. B. Mallion, Hückel Theory for Organic Chemists. *Academic Press.* 1978.

[2] O. Kahn, Molecular Magnetism. *John Wiley & Sons*. 1993

[3] P. J. Hay, J. C. Thibeault, R. Hoffmann, Orbital Interactions in Metal Dimer Complexes. *J. Am. Chem. Soc*. 1975, **97**, 4884–4899.